Spatial optical solitons in highly nonlocal media

Alessandro Alberucci, Chandroth P. Jisha, Noel F. Smyth, and Gaetano Assanto

Phys. Rev. A **91**, 013841 — Published 27 January 2015

DOI: 10.1103/PhysRevA.91.013841

Spatial optical solitons in highly nonlocal media

Alessandro Alberucci,[1,*] Chandroth P. Jisha,[2] Noel F. Smyth,[3] and Gaetano Assanto[1,4]

[1] ***NooEL*** *- Nonlinear Optics and OptoElectronics Lab, University "Roma Tre", 00146 Rome - Italy*
[2] *Centro de Física do Porto, Faculdade de Ciências, Universidade do Porto, R. Campo Alegre 687, Porto 4169-007, Portugal*
[3] *School of Mathematics, University of Edinburgh, The King's Building, Edinburgh, Scotland EH9 3FD, U.K.*
[4] *Optics Laboratory, Tampere University of Technology, FI-33101 Tampere, Finland*

We theoretically investigate the propagation of bright spatial solitary waves in highly nonlocal media possessing radial symmetry in a three-dimensional cylindrical geometry. Focusing on a thermal nonlinearity, modeled by a Poisson equation, we show how the profile of the light-induced waveguide strongly depends on the extension of the nonlinear medium in the propagation direction as compared to the beam width. We demonstrate that self-trapped beams undergo oscillations in size, either periodically or aperiodically, depending on the input waist and power. The —usually neglected— role of the longitudinal nonlocality, as well as the detrimental effect of absorptive losses, are addressed.

I. INTRODUCTION

Light beam self-localization in nonlinear nonlocal materials, that is, in the presence of a nonlinearly induced refractive index well extending beyond the beam profile, has been widely investigated in the last few years, both experimentally and theoretically. A nonlocal response allows for the stabilization of bright $(2+1)$D spatial solitons, at variance with the collapse observed in local Kerr media (Townes soliton) [1–3]. In fact, self-localization of light and, specifically, the soliton profile and its stability, all strongly depend on the degree of nonlocality [4]. Nonlocality also entails the observation of phase-insensitive long-range interactions between solitons [5, 6], stable propagation of higher order solitons [7–11], thresholdless surface solitons [12], power-dependent steering due to interaction with boundaries [13–15], and so on. Moreover, modeling spatial solitons in the highly nonlocal limit leads to the concept of accessible solitons [16], a useful approximation in various instances [17–19]. Nonlocality in optics also plays an important role in photon condensation [20], dispersive shock waves [21–23], distributed coupling to guided-waves [24, 25], gradient catastrophe [26] and Anderson localization [27].

Several optical materials exhibit a highly nonlocal nonlinearity, often related to diffusive processes. Accessible solitons were first reported in nematic liquid crystals [17], with self-focusing provided by molecular reorientation [28] and nonlocality stemming from intermolecular forces [29]. High nonlocality in soliton propagation has also been exploited in thermo-optic media (heat diffusion ruled by a Poisson equation) [7, 30, 31], atomic vapors (molecular diffusion) [32], photorefractive crystals [33], semiconductors [34] (carrier diffusion), nanoparticle suspensions (thermophoresis) [35], silica nanowebs (optomechanics) [36] and colloidal suspensions (optical gradient forces) [37].

* Corresponding author: alessandro.alberucci@gmail.com

From a theoretical viewpoint, most highly nonlocal materials can be modeled by a diffusion-like equation describing the light-induced refractive index distribution. With a few exceptions in reorientational liquid crystals [38–40], however, longitudinal nonlocal effects are usually neglected, that is, the Laplacian operator lacks the partial derivative along the propagation direction. This is appropriate only for shape-preserving beams and/or in the absence of power dissipation; even without losses, in fact, the family of self-confined waves includes breathing solitons subject to bounded periodic oscillations of their width and peak intensity [16, 17, 41–43]. In such cases the refractive index gradient along the direction of propagation affects the self-trapped wavepacket. Additionally, when losses are included, a longitudinal gradient arises even when a shape-preserving soliton is launched at the input [21, 44]: appreciable effects are expected when the attenuation distance is comparable with the Rayleigh length of the input beam.

In this Paper we study light propagation in a highly nonlocal, nonlinear medium in a 3D cylindrical geometry with circular symmetry. The nonlinear, nonlocal refractive index well is accounted for by a Poisson equation, which applies to actual highly nonlocal materials and systems [19, 45]. We first show that the nonlinear lens induced by a light beam strongly depends on the ratio between the input radius and the available propagation length. We then discuss how the light-induced refractive index well affects light propagation, with particular attention to the beam width. We also address the roles of the longitudinal nonlocality and of the unavoidable absorptive losses, two important aspects usually ignored in literature. The paper is organized as follows. In Section II we introduce the mathematical model and its range of applicability. In Section III we compute the nonlinear perturbation, keeping fixed the optical excitation and using a Green's function formalism. In Section IV we employ Beam Propagation Method (BPM) simulations to account for the effect of the nonlinear refractive index well on beam propagation. Finally, in Section V

we summarize the results and pinpoint further developments.

II. MODEL

Let us consider a thermo-optic medium with heat transfer dominated by conduction. We take a homogeneous cylinder of circular cross-section, diameter $2a$ and length l in z, with a radially symmetric input beam launched in $z = 0$ and centered in $r = 0$ (r is the radial coordinate). Light propagation in the paraxial, slowly varying envelope approximation and for small nonlinear index changes is governed by

$$2ik_0n_0\frac{\partial A}{\partial z} + \frac{1}{r}\frac{\partial}{\partial r}\left(r\frac{\partial A}{\partial r}\right) + 2n_0k_0^2\phi A + ik_0n_0\alpha A = 0, \tag{1}$$

$$\gamma\frac{\partial^2\phi}{\partial z^2} + \frac{1}{r}\frac{\partial}{\partial r}\left(r\frac{\partial\phi}{\partial r}\right) = -\alpha|A|^2, \tag{2}$$

where A is the beam envelope (normalized so that $I = |A|^2$ is the intensity), k_0 is the vacuum wavenumber, n_0 is the linear refractive index, $\alpha > 0$ is the absorption coefficient, $\phi = n(r, z, P) - n_0$ is the nonlinear (i.e., power-dependent) refractive index well, with $P(z) = 2\pi\int|A|^2rdr$ the beam power at each section z. The constant γ "turns on (off)" the longitudinal nonlocality when set equal to 1 (0). Equation (2) is solved together with the boundary conditions $\phi(r = a, z) = \phi(r, z = 0) = \phi(r, z = l) = 0$, valid irrespective of the power P. Without loss of generality, in writing Eq. (2) we assumed that the thermal conductivity and capacity are both equal to 1; moreover, we assumed that the thermo-optic coefficient is unitary as well, i.e., $\phi = \Delta T = T - T_0$, with T the local temperature and T_0 the environment (background) temperature. In the general case the thermal conductivity of the medium, providing the proportionality factor between heat flux and temperature gradient, would multiply the whole LHS of Eq. (2); in a similar way, the RHS of Eq. (2) should be multiplied by the thermal capacity of the material. We note that the model consisting of Eqs. (1)–(2) is quite general, as it can also describe, e.g., particle diffusion and weak all-optical reorientation in liquid crystals [39]. Finally, this set of equations can be normalized by scaling all the spatial dimensions (including the wavelength λ and the absorption distance $1/\alpha$) with the medium extension l along z, provided the beam power P is multiplied by l.

III. NONLINEAR WELL FOR A GIVEN INTENSITY PROFILE

We first discuss how the nonlinear refractive index well Δn (corresponding to ϕ in our formalism) changes for a fixed excitation I. For the sake of simplicity, in the following we assume an infinitely extended cylinder, that is, $a \to \infty$.

A. Green's function

Writing ϕ in terms of its own Hankel transform, Eq. (2) for $\gamma = 1$ becomes the ordinary differential equation

$$\frac{\partial^2\tilde{\phi}}{\partial z^2} - k_r^2\tilde{\phi} + \alpha\tilde{I} = 0, \tag{3}$$

with $\tilde{\phi}(k_r, z) = \int_0^\infty r\phi(r, z)J_0(k_rr)dr$ the Hankel transform of ϕ. A general description (magnitude, longitudinal and transverse width) of the solutions of Eq. (2), in particular their dependence on the boundary conditions across z, can be obtained using a Green's function. Setting $I = \delta(r - r')\delta(z - z')/(2\pi r)$ [(r', z') is the location of the impulsive ring-like excitation], the corresponding distribution of the index of refraction reads

$$\phi_{ring}(r, r', z, z') = -\alpha\left[G_{ring}(r, r', z, z') + G_{ring}(r', r, z', z)\right], \tag{4}$$

having defined the auxiliary function

$$G_{ring}(r, r', z, z') = u_0(z' - z)u_0(l - z')\times \int_0^\infty \frac{J_0(k_rr)J_0(k_rr')}{\sinh(k_rl)}\sinh\left[k_r\left(z' - l\right)\right]\sinh(k_rz)dk_r. \tag{5}$$

with u_0 the Heaviside step function. For $l \to \infty$ Eq. (5) gives $G_{ring} = -u_0(z' - z)\int_0^\infty J_0(k_rr)J_0(k_rr')e^{-k_rz'}\sinh(k_rz)\,dk_r$.

The overall nonlinear perturbation of the refractive index is given by the convolution of the intensity profile I with the Green's function (4): profile and size (that is, nonlocal response [39]) can be determined from the spatial behavior of ϕ_{ring}. The function ϕ_{ring} is plotted in Fig. 1 for the case $r' = 0$, i.e., a ring-like excitation degenerating to a point-source. At $r = r'$ the azimuthally-averaged impulsive response ϕ_{ring} is singular, in agreement with the general properties of the Poisson's equation. Clearly ϕ_{ring} has a finite extent related to the nonlocal response along z, with size approximately equal to $0.1l$. Due to this finite size along z, the system response depends on z' and gets smaller and strongly asymmetric near the boundaries [Fig. 1(a)]. The spatial size of the response along r is comparable with the nonlocality along z: the longitudinal boundary conditions fix the transverse nonlocality as well, as $l \ll a$ in this case (see Ref. [46] for a similar case in a rectangular 2D geometry). Finally, Fig. 1(b) graphs the system response in the limit $l \to \infty$: ϕ_{ring} tends to the free space solution for $z' > 1/2$ due to the absence of the output interface.

B. Gaussian excitation

The influence of nonlocality on light propagation is maximum in the highly nonlocal case: solitons acquire

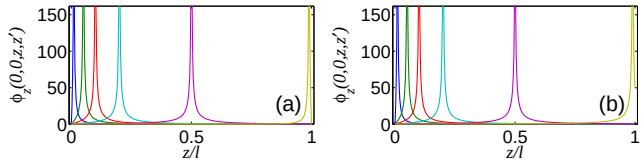

FIG. 1. (Color online) (a) Function ϕ_{ring} versus z/l and in $r = 0$ for excitations placed on the symmetry axis (i.e., $r' = 0$); the curves from left to right correspond to $z' = 0.01l$, $0.05l$, $0.1l$, $0.2l$, $0.5l$ and $0.99l$, respectively. (b) Same as in (a), but for an infinite propagation length l. In the plot we set $l = 1$ for a direct comparison with panel (a).

nearly Gaussian profiles [16, 19], with a varying width w along z due to breathing and/or power losses. Thus we write

$$I = \frac{2P_0}{\pi w^2(z)} e^{-\frac{2r^2}{w^2(z)}} e^{-\alpha z} = I_0(z) e^{-\alpha z} e^{-\frac{2r^2}{w^2(z)}}, \qquad (6)$$

with P_0 the initial power at $z = 0$. Then we substitute the ansatz (6) into (2) in order to find the perturbation ϕ corresponding to a given intensity distribution I. Using the Green function ϕ_{ring} we find that

$$\phi(r,z) = \int_0^\infty r'dr' \int_0^l I(r',z')\phi_{ring}(r,r',z,z')dz'. \qquad (7)$$

In Eq. (7) ϕ is computed [with Eq. (5)] by evaluating a triple integral. The integration along r', expressed as $F(k_r,w) = \int_0^\infty r' I(r',z') J_0(k_r r')dr'$, can be performed first: F is the Hankel transform of I and contains information on the spatial extension of the beam (in fact, all terms depending on the beam size $w(z)$ are included in it). When I is radially Gaussian as in Eq. (6), we obtain $F(k_r,z,w) = (w^2/4)I_0(z)\exp(-\alpha z)\exp\left(-k_r^2 w^2/8\right)$.

1. *Constant width*

The simplest case is when the beam size $w(z)$ is constant along z. The solution of Eq. (2) is

$$\phi(r,z) = -\alpha \int_0^\infty \frac{J_0(k_r r)}{\sinh(k_r l)} H(k_r,z) F(k_r,z,w) dk_r, \quad (8)$$

where

$$H = \left[e^{-k_r l}\frac{e^{(k_r-\alpha)l} - e^{(k_r-\alpha)z}}{2(k_r-\alpha)} - e^{k_r l}\frac{e^{-(k_r+\alpha)z} - e^{-(k_r+\alpha)l}}{2(k_r+\alpha)}\right]\sinh(k_r z) + \left[\frac{e^{(k_r-\alpha)z}-1}{2(k_r-\alpha)} - \frac{1-e^{-(k_r+\alpha)z}}{2(k_r+\alpha)}\right]\sinh[k_r(z-l)]. \qquad (9)$$

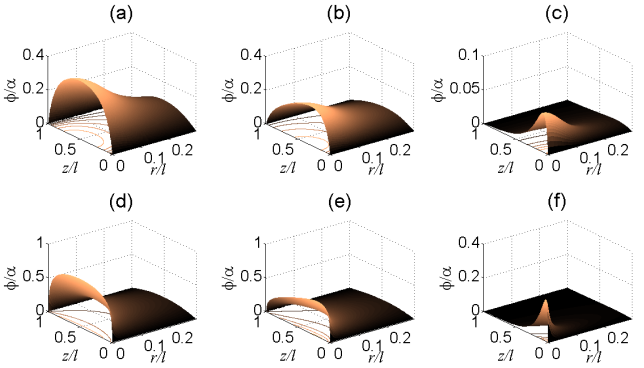

FIG. 2. (Color online) Plot of ϕ computed from Eq. (8) normalized to the absorption α versus r/l and z/l for $w/l = 0.1$ (a)–(c) and $w/l = 0.01$ (d)–(f); normalized absorption coefficients αl are 1×10^{-15} (a,d), 1 (b,e) and 10 (c,f). Input power P_0 is the same regardless of the beam spot.

The correctness of Eqs. (8)–(9) was verified by a direct comparison with the numerical solutions of Eq. (2) obtained via standard relaxation algorithms. We note that, for large k_r, it is $H/\sinh(k_r l) \approx -\exp(-\alpha z)/k_r$, thus ensuring the convergence of the integral (8) for finite w.

Figure 2 shows a few examples of the nonlinear refractive index well ϕ computed from Eq. (8). The most striking difference from the local case $\gamma = 0$ is the role of input and output interfaces on ϕ, with the formation of a transition region between the boundary and the bulk; in fact, in the approximation $\gamma = 0$ it is implicitly assumed that light propagates in bulk, that is, without effects from the end-faces along the propagation direction z. For small absorption α the light-induced perturbation is almost symmetric with respect to the transformation $z \to z - l$, whereas increased losses lead to a marked asymmetry between input and output, as is physically apparent. As expected, ϕ also depends on the beam width w. For narrow beams the transition between the interfaces and the bulk region is much steeper than for wide beams: in fact, for small w the derivative along r is dominant with respect to z, thus the longitudinal effects can be neglected over a wider region.

The role of the transverse I profile on ϕ (i.e., on the beam width w if we consider a Gaussian input) can be addressed by looking at Eq. (8) or at Fig. 3, where $H/\sinh(k_l r)$ is graphed. The auxiliary function $H_{\rm aux} = H(k_r, z/l)/\sinh(k_r l)$ vanishes on line $k_r = 0$, reaching a peak for a finite k_r and then monotonically decreases (Fig. 3). In z the function $H_{\rm aux}$ has a sine-like

behavior for small absorption, but shows a strong peak close to the input interface for large losses [Fig. 3(a)–(c)], in full analogy with the behavior of ϕ in Fig. 2. Noteworthy, the width of $H_{\rm aux}$ on the k_r axis becomes larger as α increases. The net effect on ϕ can be understood by examining Figs. 3(d)–(e). For wide beams the Hankel transform F tends to a Dirac delta, so that the integral is sampled in $k_r = 0$: this implies a smaller perturbation ϕ (compare the two rows in Fig. 2) and an effective cut-off for high spatial frequencies k_r, thus inhibiting rapid variations of ϕ. Conversely, for narrow beams the Hankel transform F acts as a weight function with a width inversely proportional to w. Thus, the narrower the excitation I the larger the cut-off frequency in k_r is: ϕ can vary on short spatial lengths, in agreement with Fig. 2.

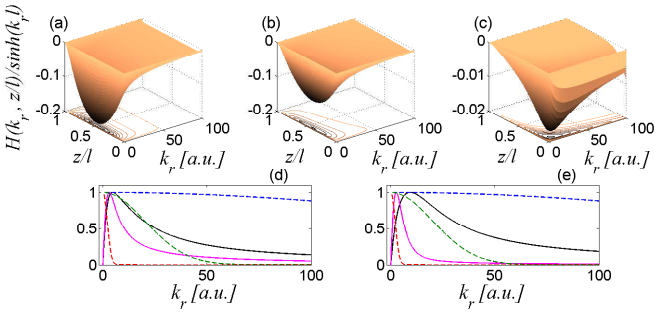

FIG. 3. (Color online) $H_{\rm aux}$ in the plane $(k_r, z/l)$ for $\alpha l = 1 \times 10^{-15}$ (a), 1 (b) and 10 (c). Sections of $|H_{\rm aux}|$ versus k_r for $\alpha l = 1$ (d) and $\alpha l = 10$ (e); the $z-$coordinates are 0.11 (black solid lines, correspoding to the widest curves) and 0.5 (magenta solid lines, corresponding to the narrowest curves). Dashed lines in (d,e) are the Hankel trasform $F(k_r, w)$ of I for $w/l = 0.01$ (blue dashes) 0.1 (green dashes) and 1 (red dashes), from the widest to the narrowest, respectively.

The advantage of an integral solution like Eq. (8) with respect to a direct numerical solution of Eq. (2) is the possibility of computing the perturbation ϕ and its derivative in a given portion of space (in our case the line $r = 0$) without the need for a complete knowledge of ϕ. In fact, in the limit of high nonlocality the two quantities required to compute soliton propagation are the perturbation peak $\phi_0(z) = \phi(r = 0, z)$ and the Taylor series coefficient $\phi_2(z) = \partial^2\phi/\partial r^2(r = 0, z)$, the latter giving the strength of the nonlinear refractive index well [16].

Having calculated the longitudinally nonlocal case $\gamma = 1$, the next step is to obtain the nonlinear perturbation ϕ when $\gamma = 0$, i.e., for a longitudinally local nonlinearity. In this case, we need to fix a finite a to ensure a finite ϕ; we take $a = Nw$. Integrating Eq. (2) twice yields $\phi_0 = \frac{\alpha P_0}{2\pi} T(N) e^{-\alpha z}$, with $T(N) = \int_0^N dt \left(1 - e^{-2t^2}\right)\Big/ t$: the peak of the perturbation depends on the boundary condition via the parameter N, tending to infinity for N arbitrarily large. Furthermore, using the Taylor expansion around $r = 0$ we find [18]

$$\phi_2 = -\frac{\alpha P_0}{2\pi w^2} e^{-\alpha z}. \tag{10}$$

Figure 4(a) shows the numerically computed ϕ along $z = 0$ for $\gamma = 0$: as anticipated, the peak of the nonlinear perturbation ϕ_0 is roughly proportional to $\log N$. The inset compares the full profile and the approximation with a parabolic nonlinear index well: the accuracy worsens for $r \approx w$, in agreement with Ref. [45]. We then compare the approximate solution for $\gamma = 0$ with the exact profile for $\gamma = 1$ above. The effect of the longitudinal nonlocality on ϕ reduces as the width w/l becomes smaller: in this regime, in fact, the transverse derivative along r is dominant [Fig. 4(b)–(c)]. Importantly, the differences between the local and the nonlocal cases are bigger for the amplitude perturbation ϕ_0 than for ϕ_2. In agreement with the Green's function in Fig. 1, the case $\gamma = 0$ cannot describe the effects of input and output facets on the overall distribution of ϕ, whereas it faithfully reproduces the decay in z due to a non-zero α. Finally, Fig. 4(d) shows the behavior of the normalized maximum nonlinear perturbation ϕ versus normalized absorption: the smaller w, the stronger the normalized nonlinear perturbation is, unlike the original model proposed by Snyder and Mitchell which assumes a nonlinear refractive index well depending on the beam power only [16].

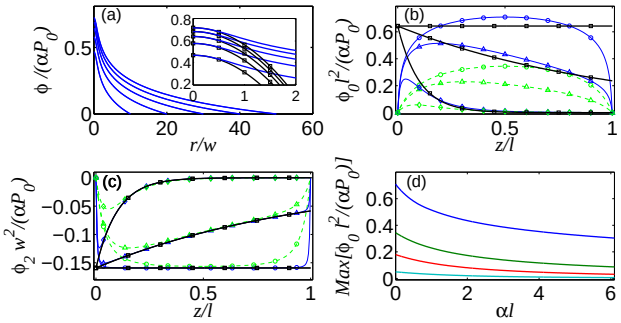

FIG. 4. (Color online) (a) Normalized nonlinear perturbation ϕ versus r/w in the local case $\gamma = 0$ and $z = 0$; each curve corresponds to a different N, uniquely identified by the point where ϕ vanishes. Plots of the normalized (b) ϕ_0 and (c) ϕ_2 versus z/l for $\gamma = 1$ when $w/l = 0.01$ (blue solid lines) and when $w/l = 0.1$ (green dashed lines); absorption coefficient αl is 1×10^{-15} (circles), 1 (triangles) and 10 (diamonds). Black lines with squares refer to the local case for the same set of αl. (d) Maximum normalized ϕ_0 versus αl for $w/l = 0.01$, 0.1 , 0.3 and 1 for $\gamma = 1$, from top to bottom curves, respectively.

2. *Sinusoidal breathing*

Next we consider the case of a breathing soliton, that is, with width w varying along z. We assume for the width a sinusoidal behavior of the form

$$w = w_m + \Delta w \sin\left(\frac{2\pi}{\Lambda} z\right), \tag{11}$$

where w_m is the mean beam width, Δw and Λ are the breathing oscillation amplitude and period, respectively. The peak of the perturbation ϕ_0 versus z characterizes the nonlinear refractive index well written by a breathing soliton obeying Eq. (11). In order to quantify the effects due to width modulation, we define $\Delta\phi_0$ as the relative change in ϕ_0 with respect to the case $\Delta w = 0$ (lack of breathing):

$$\Delta\phi_0(z, w_m, \Delta w, \Lambda) = \frac{\phi_0(z, w_m, \Delta w, \Lambda)}{\max_z\left[\phi_0(z, w_m, \Delta w = 0, \Lambda)\right]}, \tag{12}$$

where $\max_z$ indicates the maximum computed along the z axis.

In the local case $\gamma = 0$, both ϕ_0 and ϕ_2 retain the same form as in the case of a $z-$independent beam, as the nonlinear perturbations ϕ computed in different sections are independent from each other: in other words, the nonlinear perturbation follows the beam width oscillation, despite how large the amplitude Δw or how short the period Λ are.

Figure 5 shows ϕ_0 versus z, computed from Eq. (7) after setting $r = 0$: generally, $\Delta\phi_0$ mimicks the sinusoidal behavior of the beam width w, with a non-zero mean value owing to the nonlinear relationship between w and I. Clearly, the perturbation of ϕ depends on how w varies with z: a faster modulation of w along z yields a slightly smaller perturbation $\Delta\phi_0$ due to the smoothing action of ϕ_{ring} (compare first and second rows in Fig. 5). Moreover, the relative modulation of $\Delta\phi_0$ is proportional to $\Delta w/w_m$ with good accuracy (compare first and third rows in Fig. 5): in fact, the intensity I is proportional to w^{-2}, thus $|\Delta I|/I \propto |\Delta w|/w_m$.

The quantity ϕ_0 has a minor role in beam self-confinement: it produces a power-dependent modulation of the effective propagation constant of the self-trapped beam, the latter having relevance only when the solitary wave interferes with a reference beam [47]. The parameter ruling the beam width is ϕ_2, quantifying the strength of the self-induced index well. If the field intensity is given by Eq. (6), Eqs. (5) and (7) yield

$$\phi_2(z) = \frac{\alpha P_0}{4\pi}\int_0^\infty \frac{k_r^2 dk_r}{\sinh(k_r l)}\int_0^l g(z,z')e^{-\alpha z'}e^{-\frac{k_r^2 w^2}{8}}dz', \tag{13}$$

where we set

$$\begin{aligned} g(z,z') =& \sinh(k_r z)\sinh\left[k_r(z'-l)\right]u_0(z'-z) \\ &+ \sinh(k_r z')\sinh\left[k_r(z-l)\right]u_0(z-z'). \end{aligned} \tag{14}$$

The results computed from Eq. (13) are presented in Fig. 6. First, due to the linearity of Eq. (2), the parameter ϕ_2 is inversely proportional to w_m^2. Nonetheless, the shape of ϕ along z strongly depends on the ratio w_m/l. For small w_m/l the periodic modulation of the nonlinear well is retained, approaching the local limit $\gamma = 0$ (black curves with symbols in Fig. 6) as w_m/l reduces; conversely, for large w_m/l the oscillations in z are smoothed out. The size of ϕ_2 increases with $\Delta w/w_m$, similar to ϕ_0; moreover, the spatial filtering of the longitudinal oscillations of ϕ_2 changes slightly with $\Delta w/w_m$, with an appreciable difference between the local case [Eq. (10)] and the case $w_m/l = 0.01$, arising only for $\Delta w/w_m > 0.2$. Finally, a direct comparison between the first and second columns in Fig. 6 shows that ϕ_2 is nearly independent of the oscillation period Λ.

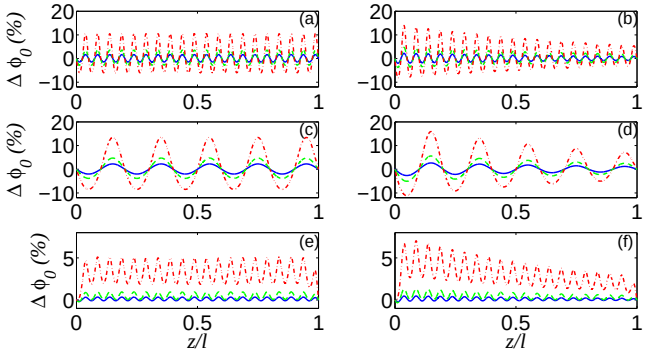

FIG. 5. (Color online) $\Delta\phi_0$ versus z/l for an averaged waist $w_m/l = 0.01$ (a)–(d) and $w_m/l = 0.1$ (e)–(f); the breathing period is $\Lambda/l = 0.05$ (a,b,e,f) and $\Lambda/l = 0.1$ (c,d). On the left (a,c,e) and right (b,d,f) column the normalized losses αl are 1×10^{-15} and 1, respectively. The normalized oscillation amplitude $\Delta w/w_m$ is 0.1 (blue solid lines), 0.2 (green dashes) and 0.5 (red dash-dotted lines), respectively.

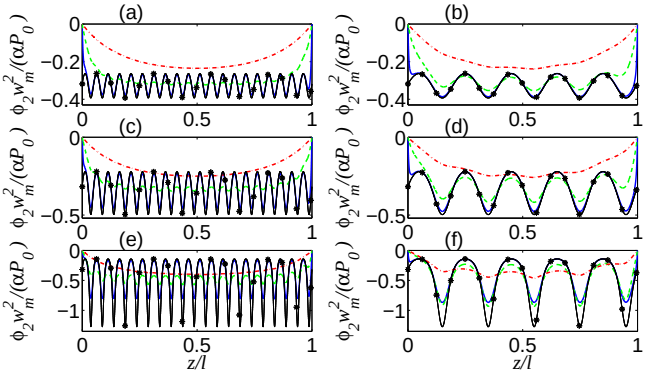

FIG. 6. (Color online) $\phi_2 w_m^2/(\alpha P_0)$ versus z/l for $\Delta w/w_m = 0.1$ (a)–(b), 0.2 (c)–(d) and 0.5 (e)–(f); left (a,c,e) and right (b,d,f) columns correspond to $\Lambda/l = 0.05$ and 0.2, respectively. The mean waist w_m/l is 0.01 (blue solid lines), 0.1 (green dashes) and 0.5 (red dash-dotted lines). Black lines with symbols refer to the local case given by Eq. (10). Here we set $\alpha l = 1\times10^{-15}$.

IV. NONLINEAR LIGHT PROPAGATION

Up to now we have calculated the nonlinear refractive index well determining the intensity distribution I: next we numerically solve Eq. (1) together with the constitutive equation (2). The numerical algorithm to compute the wavepacket evolution is based on a Finite Difference Beam Propagation Method. In the longitudinal case $\gamma = 1$, we firstly find the beam evolution for a given distribution of the refractive index ϕ, then we substitute the corresponding intensity I into Eq. (2); this procedure is iterated until we achieve convergence. For $\gamma = 0$ the algorithm is slightly different: the beam intensity in a plane z = constant is used to find the corresponding nonlinear refractive index well through Eq. (2); the latter well is then used to calculate the new field profile in the following section.

A. Profile-invariant solitons

The first goal consists in determining the steady solitary wave solution which preserves its profile while propagating in the z direction. Since losses prevent the propagation of truly invariant wavepackets, we initially set $\alpha = 0$ in Eq. (1) to calculate the shape-preserving solitary waves and, then, we include attenuation and compute (numerically) their evolution in the absorbing sample. Setting $\phi = v(r)$ and $A = u(r)e^{i\beta z}$ (u can be taken real without loss of generality) Eqs. (1)–(2) yield

$$\beta u = \frac{1}{2k_0 n_0}\frac{1}{r}\frac{\partial}{\partial r}\left(r\frac{\partial u}{\partial r}\right) + k_0 v u, \tag{15}$$

$$\alpha u^2 = -\frac{1}{r}\frac{\partial}{\partial r}\left(r\frac{\partial v}{\partial r}\right), \tag{16}$$

as the equations for a steady solitary wave.

Fundamental (single-humped) solitary wave solutions of Eqs. (1)–(2) are plotted in Fig. 7. The solutions can be normalized by introducing the scaled radial coordinate $R = k_0 r$, the scaled propagation constant $N_{\rm eff} = \beta/k_0$ and the scaled power $\mathcal{P} = \alpha P$. The solutions of the system (1)–(2) strongly depend on the chosen radius r_0 for the integration domain: here we take $r_0 = 50/k_0$ and limit our considerations to normalized soliton widths $W = wk_0$ of a few units, so that the finite boundaries do not affect the results [see Fig. 4(a)]. The soliton profiles across r are nearly Gaussian, but their width is $\sqrt{2}$ larger than that steming from the Snyder-Mitchell model [19], the latter providing the condition $\alpha P w^2 k_0^2 = 8\pi$ for the existence of shape preserving solitary waves [16]: this discrepancy is due to the singularity (at the origin) of the response function used here, whereas the Snyder-Mitchell model assumes it is continuous and differentiable everywhere in space [19, 45]. In summary, the width w_s of the Gaussian best-fit to the soliton profile is expressed by

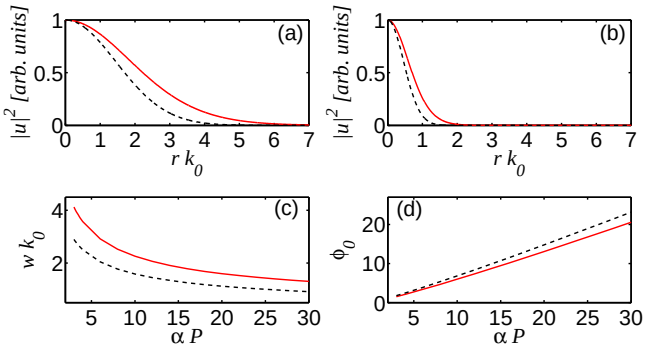

FIG. 7. (Color online) Soliton profile $|u|^2$ normalized to its own peak versus normalized radial distance rk_0 for (a) $\alpha P = 3$ and (b) $\alpha P = 30$, respectively; (c) normalized soliton width wk_0 and (d) peak of the nonlinear perturbation ϕ_0 versus normalized power αP. In all panels red solid lines and black dashes correspond to exact numerical solutions and predictions of the original Snyder-Mitchell model, respectively (see Ref. [19] for a deeper insight).

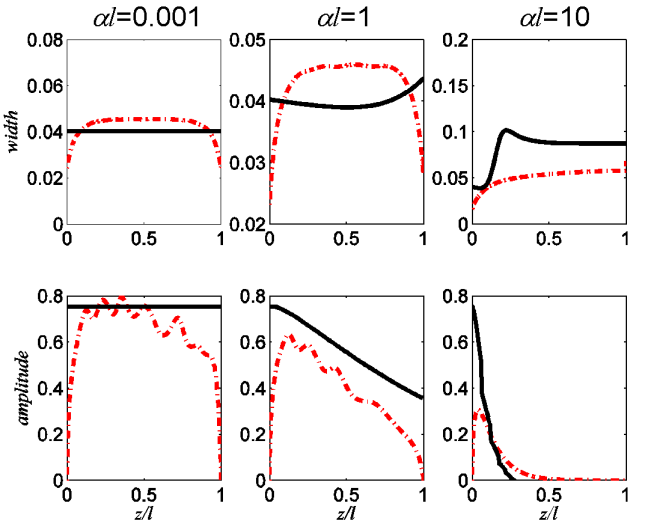

FIG. 8. (Color online) z Evolution of width (top) and amplitude (bottom) of the nonlinear potential ϕ for absorption coefficients αl as marked. The solid lines refer to the longitudinally-local case $\gamma = 0$, whereas the dotted lines represent the full 3D nonlocal case. Here $\alpha P_0 = 1.5$ is kept constant and $\lambda/l = 0.02$.

$$w_s(P) = \sqrt{\frac{16\pi}{k_0^2 \alpha P}}. \tag{17}$$

Next we address the effect of absorption losses when solitary waves are launched at the input $z = 0$. We expect that shape variations, linked to the power decay along z, become more relevant as α increases. Figure 8 shows the width and amplitude of the nonlinear potential as obtained from BPM simulations. The beam profile

remains almost unaltered for a longitudinally local nonlinearity ($\gamma = 0$) when αl is much less than unity (negligible losses), with an associated nonlinear potential which is uniform along the sample (solid lines). As αl becomes comparable to 1, self-trapping fades out, allowing light diffraction and exponential decay along z. The results in the longitudinally nonlocal case $\gamma = 1$ (dashed lines) are more intriguing: due to the boundary condition at the input facet, the beam amplitude undergoes appreciable oscillations along z even for small αl. In fact, the boundaries at $z = 0$ and $z = l$ break the longitudinal symmetry and inhibit the existence of shape preserving solitons, no matter how small the losses are. The deviation from the longitudinally invariant solution is more appreciable when the perturbed interface region is longer than the Rayleigh distance of the input beam with a solitary wave profile, so that oscillations are expected to increase with input power.

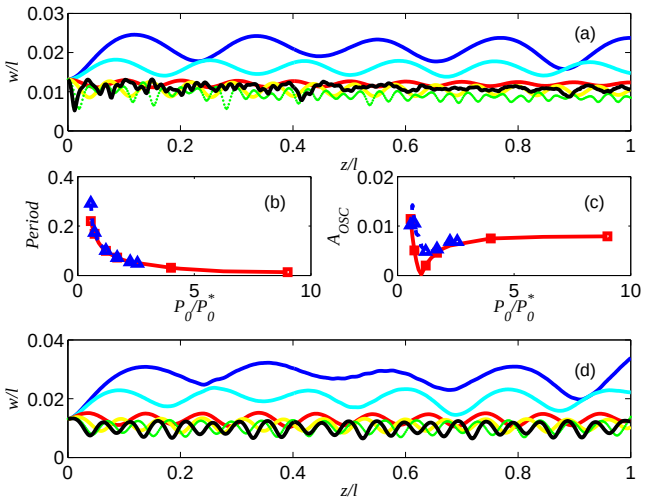

FIG. 9. (Color online) Beam width vs z/l for powers P_0 differing from the soliton power $P_0^\star$ for (a) the local case [$P_0/P_0^\star$ equals 0.56 (blue line), 0.72 (cyan line), 1.21 (red line), 1.69 (yellow line), 4 (green line) and 9 (black line)] and (d) the nonlocal case [$P_0/P_0^\star$ is 0.56 (blue line), 0.72 (cyan line), 1.21 (red line), 1.69 (yellow line), 2.25 (green line) and 2.56 (black line)]; beam focusing increases with P_0 (top to bottom). (b) Corresponding oscillation period and (c) oscillation amplitude for varying P_0; symbols correspond to the excitations in (a)–(d). Solid lines with □ refer to the local case and dashed lines with △ to the nonlocal one. At high powers, in the local case the sinusoidal behavior is lost whereas in the nonlocal case the solutions do not converge (not shown). Here $\alpha l = 1 \times 10^{-15}$, $P_0 = 1.23 \times 10^9$ and $\lambda/l = 0.02$.

B. Breathing solitons

The most general self-localized waves are breathing solitons, that is, spatially localized beams undergoing transverse shape changes in propagation due to the interplay between diffractive spreading and self-focusing [16]. In this subsection we will discuss their features.

1. *Ehrenfest's theorem for beam width*

Using a straightforward generalization of Ehrenfest's theorem a simple ordinary differential equation is found to govern the beam width evolution due to the competition between diffraction and self-focusing. For a parabolic index well the beam width obeys [48]

$$\frac{n_0}{2}\frac{d^4w^2}{dz^4} - 2\phi_2\frac{d^2w^2}{dz^2} - 3\frac{d\phi_2}{dz}\frac{dw^2}{dz} - \frac{d^2\phi_2}{dz^2}w^2 = 0, \quad (18)$$

where ϕ_2 generally depends on z due to losses ($\alpha \neq 0$) or breathing.

When the changes in beam width are negligible and $\alpha l \ll 1$, according to Eq. (10) the variation of ϕ_2 with z is negligible: in this limit Eq. (18) is linear in the unknown variable w^2 and its solution is

$$\frac{w^2}{w_0^2} = 1 + \frac{w_s^4 - w_0^4}{2w_0^4}\left[1 - \cos\left(\sqrt{\frac{4|\phi_2(P_0)|}{n_0}}z\right)\right], \quad (19)$$

with ϕ_2 computed for the soliton case, thus depending only on the input power P_0. In deriving Eq. (19) we set $w(z = 0) = w_0$ and assumed $dw^2/dz = 0$ at $z = 0$ (i.e., a flat phase profile at the input). In this limit ϕ_2 is fixed by the input power and takes the form $\phi_2(P) = -\alpha P/(2\pi w_s^2) = -k_0^2\left(\alpha P\right)^2/(32\pi^2)$ [see Eqs. (10) and (17)]. The breathing period is then $\Lambda = 4\sqrt{2n_0}\pi^2/(k_0\alpha P)$.

When ϕ_2 changes slowly with z due to losses, Eq. (19) predicts adiabatic variations in both breathing amplitude (determined by the ratio between w_0 and w_s, thus generally non-monotonic with z) and period Λ (monotonically increasing with z).

When the derivatives of ϕ_2 with respect to z cannot be neglected (w_0 appreciably differing from w_s), we can substitute Eq. (10)— valid away from the interfaces for narrow beams with $\gamma = 1$ (see Fig. 6)— into Eq. (18), yielding

$$\frac{n_0}{2}\frac{d^4w^2}{dz^4} + \frac{\alpha P_0 e^{-\alpha z}}{2\pi w^2}\frac{d^2w^2}{dz^2} - \frac{\alpha P_0 e^{-\alpha z}}{2\pi w^4}\left(\frac{dw^2}{dz}\right)^2 = 0. \quad (20)$$

Equation (20) is highly nonlinear, in general with aperiodic solutions. To this extent and for the sake of simplicity, we neglect the last term in Eq. (20), i.e. we leave out very narrow solitons. Therefore, Eq. (20) becomes harmonic (with respect to the unknown d^2w^2/dz^2), but with an oscillation period proportional to the width w. Changes in beam width imply variations in periodicity, in turn leading to a rather aperiodic breathing.

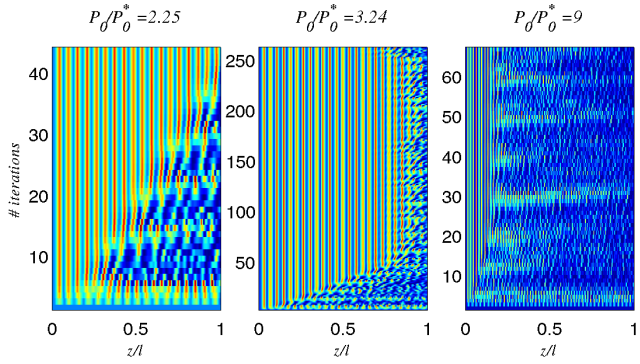

FIG. 10. (Color online) Beam evolution in $r = 0$ vs z/l at various steps of the iteration for the nonlocal case discussed in Fig. 9. Relaxation is achieved at low input powers (see results for $P_0/P_0^\star = 2.25$), whereas the code does not converge for high P_0 (see results for $P_0/P_0^\star = 3.24$, 9).

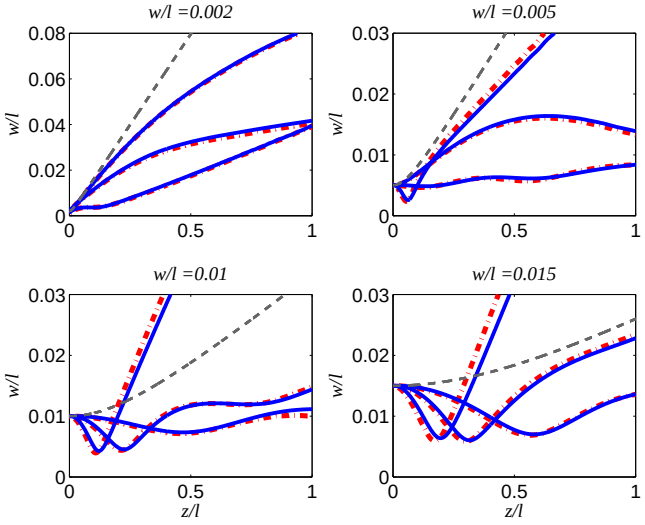

FIG. 11. (Color online) Beam width vs z for a Gaussian input; each panel corresponds to a different input waist, as marked. The curves correspond to $\alpha P_0 = 0.01$ ($\alpha l = 1 \times 10^{-15}$), $\alpha P_0 = 0.03$ ($\alpha l = 1$) and $\alpha P_0 = 0.12$ ($\alpha l = 10$), respectively (higher αP_0 correspond to stronger focusing). Blue solid and red dash-dotted lines refer to nonlocal and local cases, respectively. Gray dashed lines represent linearly diffracting beams. Here $\lambda/l = 1 \times 10^{-3}$.

2. *Numerical simulations*

Hereby we validate our predictions on breathing by using the BPM. To verify how width oscillations depend on the soliton radius we assume negligibly small losses, i.e., $\alpha l \ll 1$. The input beam shape corresponds to a solitary wave for a given power $P_0^\star$, numerically computed from Eqs. (15)–(16) and shown in Fig. 7. In order to study the width oscillations, the input power P_0 is set different to the value $P_0^\star$ corresponding to a shape preserving solitary wave. Unless otherwise stated, we set $w_0 = w_s(P_0^\star)$ and let $w_s(P_0)$ vary freely.

The dynamics obtained for $\gamma = 0$ and for $\gamma = 1$ is summarized in Fig. 9. For input powers below $P_0^\star$ the beam radius oscillates quasi-periodically around a mean larger than w_0 as $w_s > w_0$. As P_0 approaches $P_0^\star$ the breathing is nearly sinusoidal, in agreement with Eq. (19). If the power is further increased, the breathing becomes aperiodic, consistent with Eq. (20). As expected, the computed breathing period Λ decreases with P_0^{-1}; similarly, the oscillation amplitude $A_{\rm OSC}$ (difference between maximum and minimum width values) tends to zero when the power approaches $P_0^\star$, but increases above and below $P_0^\star$. Note that the curve is not symmetric with respect to the soliton state as, for large powers, the beam cannot shrink indefinitely due to diffraction, the latter assuming a dominant role for wavelength or sub-wavelength beam sizes.

For input powers above $3P_0^\star$, the BPM for $\gamma = 0$ yields a strongly aperiodic breathing in agreement with Eq. (20). Noteworthy, the BPM solution is stable when input noise is added. In the nonlocal case ($\gamma = 1$), for large powers ($P_0 > 2.56P_0^\star$) the code, based on an iterative scheme (and thus introducing different numerical noise at each step), does not converge, see Fig. 10. This can be ascribed to the highly nonlinear character of Eq. (20) for small beam widths w, leading to chaotic dynamics. Chaotic dynamics can occur in periodically modulated waveguides, even in the linear regime [49], but in our case the longitudinal modulation is due to nonlinear effects. This interpretation is corroborated by the appearance of dips in the intensity profiles at $r = 0$, pinpointing the simultaneous excitations of several modes of the self-induced guide.

Next we focus on a more realistic excitation, a fundamental Gaussian beam launched in $z = 0$ with a planar phase front, varying both its initial waist w and power P_0. Figure 11 graphs the beam width versus z for various absorption coefficients and a fixed P_0. For small losses, the self-trapped beam is quasi-periodic, in agreement with Ref. [16, 18] and Fig. 9. When the normalized loss reaches $\alpha l = 1$, the beam widens in z due to its power dropping. For $\alpha l = 10$ the beam focuses near the entrance facet due to the stronger self-focusing associated with larger absorption. The position of the focus markedly depends on the input waist, moving away from the interface as the beams get wider. At the same time, the power decays rapidly and the nonlinear effects vanish at $z/l \approx 0.2$. At the output facet the beam is wider than in the linear limit due to the initial self-focusing. In Fig. 11 the differences between the local ($\gamma = 0$) and nonlocal ($\gamma = 1$) cases are negligible due to the smallness of w/l, in agreement with Section III.

We now turn to small losses ($\alpha l = 1 \times 10^{-15}$) in the limit $w/l \ll 1$ where, according to Fig. 6, the solutions for $\gamma = 0$ and $\gamma = 1$ should be similar. To this extent we simulate the evolution of a Gaussian beam of width $w/l = 0.005$ with or without longitudinal nonlocality.

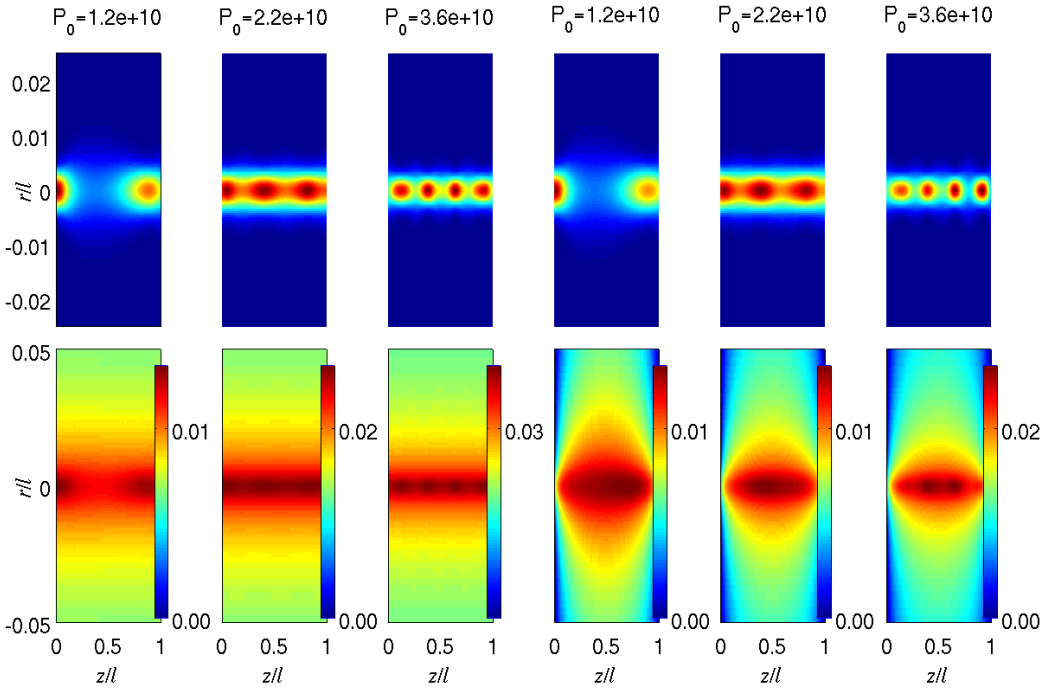

FIG. 12. (Color online) Beam evolution and corresponding index of refraction distribution for Gaussian inputs of width $w/l = 0.005$ in local (first three columns) and nonlocal regimes (last three columns), respectively, for various powers P_0. Here $\alpha l = 1 \times 10^{-15}$ and $\lambda/l = 0.02$.

Figure 12 shows the computed intensity profiles and the corresponding index of refraction distributions. As predicted by the Green's function approach, the longitudinal nonlocality does not appreciably affect the propagation in the bulk of the sample. Nonetheless, as predicted in Fig. 4, the longitudinally local case does not correctly reproduce the nonlinear refractive index well near the input and output boundaries. Thus, for instance, if long-range soliton interaction is under investigation, the local model $\gamma = 0$ is expected to overestimate the mutual attraction between solitons [6, 50].

The beam evolution is illustrated in Fig. 13. Similar to the results in Fig. 9, the oscillation period gets smaller as the power increases, whereas the oscillation amplitude is proportional to the mismatch between the input width w and the soliton width $w_s(P_0)$ for a given power P_0. We also note that the beam initially shrinks when $w > w_s$ (self-focusing overtaking diffraction), whereas the opposite occurs when $w < w_s$ (diffraction dominant on the nonlinear lens) [16, 18].

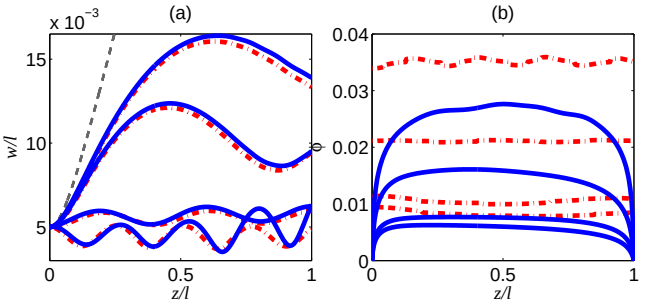

FIG. 13. (Color online) (a) Width evolution with breathing and (b) index of refraction distribution at the maximum beam amplitude for a Gaussian input and $\alpha P_0 = 0.01$, 0.012, 0.023 and 0.036 [from top to bottom in (a), in the reversed order in (b)], respectively. Solid lines correspond to the longitudinally-nonlocal case and dashed-dotted lines to the local one, respectively. Dashed gray line in (a) corresponds to linear diffraction. Here $\alpha l = 1 \times 10^{-15}$ and $\lambda/l = 1 \times 10^{-3}$.

V. CONCLUSIONS

We investigated the full 3D evolution of highly nonlocal solitons possessing radial symmetry based on a nonlinearity governed by a Poisson equation. We addressed in detail the role played by the longitudinally nonlocal response, usually neglected in literature, and the dependence of the nonlinear perturbation on the cell extension in the propagation direction. We detailed the role of longitudinal (nonlocality and attenuation) effects on the beam profile and evolution, including periodic

and aperiodic solitary-wave breathing and power attenuation. At variance with the simple case of accessible solitons [16] which oscillate sinusoidally in width and amplitude, non-exact solitary beams launched at the input tend to breathe aperiodically for input parameters away from soliton existence curve [18]. Such behavior can be qualitatively explained using Ehrenfest's theorem and a quadratic nonlinear index well.

We showed that when the nonlinearity is of thermal origin, a trade-off between the magnitude of the refractive index well and the power decay versus propagation has to be met in order to maximize beam self-trapping. Moreover, the boundary conditions break the longitudinal symmetry of the system and prevent truly shape preserving self-trapped waves from existing, even without losses.

Our model, accounting for losses and 3D nonlocality in any nonlinear regime, is a new promising workbench for studying nonlinear dynamics and the interplay of self-localization, losses and nonlocality. In its numerical implementation it is an ideal tool for the assessment of experimental results when investigating spatial optical solitons in (self-focusing) highly nonlocal media (including e.g. thermal, reorientational and liquid crystalline materials), including higher order solitons [51, 52].

Our findings can also find application in the use of Z-scan techniques [53] applied to thermal media, in the study of thermal effects in active media [54] and in the design of light-written waveguides [29], as well as for graded-index lenses in soft matter and nonlocal dielectrics.

ACKNOWLEDGEMENTS

We thank R. Barboza for enlightening discussions on log-polar coordinates for BPM computation. JCP gratefully acknowledges FCT grant n. SFRH/BPD/77524/2011 for financial support. GA acknowledges the Academy of Finland for his Finnish Distinguished Professor project, grant 282858.

[1] R. Y. Chiao, E. Garmire, and C. H. Townes, Phys. Rev. Lett. **13**, 479 (1964).
[2] D. Suter and T. Blasberg, Phys. Rev. A **48**, 4583 (1993).
[3] I. Kol'chugina, V. Mironov, and A. Sergeev, Pis'ma v Zhurnal Eksperimental'noi i Teoreticheskoi Fiziki **31**, 333 (1980).
[4] O. Bang, W. Krolikowski, J. Wyller, and J. J. Rasmussen, Phys. Rev. E **66**, 046619 (2002).
[5] M. Peccianti, K. Brzadkiewicz, and G. Assanto, Opt. Lett. **27**, 1460 (2002).
[6] C. Rotschild, B. Alfassi, O. Cohen, and M. Segev, Nat. Phys. **2**, 769 (2006).
[7] C. Rotschild, O. Cohen, O. Manela, M. Segev, and T. Carmon, Phys. Rev. Lett. **95**, 213904 (2005).
[8] S. Skupin, M. Saffman, and W. Królikowski, Phys. Rev. Lett. **98**, 263902 (2007).
[9] D. Buccoliero, A. S. Desyatnikov, W. Krolikowski, and Y. S. Kivshar, Phys. Rev. Lett. **98**, 053901 (2007).
[10] Y. V. Izdebskaya, A. S. Desyatnikov, G. Assanto, and Y. S. Kivshar, Opt. Lett. **36**, 184 (2011).
[11] Y. V. Kartashov, V. A. Vysloukh, and L. Torner, Opt. Lett. **38**, 4417 (2013).
[12] B. Alfassi, C. Rotschild, O. Manela, M. Segev, and D. N. Christodoulides, Phys. Rev. Lett. **98**, 213901 (2007).
[13] B. Alfassi, C. Rotschild, O. Manela, M. Segev, and D. N. Christodoulides, Opt. Lett. **32**, 154 (2007).
[14] A. Alberucci, M. Peccianti, and G. Assanto, Opt. Lett. **32**, 2795 (2007).
[15] F. Ye, Y. V. Kartashov, B. Hu, and L. Torner, Opt. Lett. **34**, 2658 (2009).
[16] A. W. Snyder and D. J. Mitchell, Science **276**, 1538 (1997).
[17] C. Conti, M. Peccianti, and G. Assanto, Phys. Rev. Lett. **91**, 073901 (2003).
[18] C. Conti, M. Peccianti, and G. Assanto, Phys. Rev. Lett. **92**, 113902 (2004).
[19] A. Alberucci, C. P. Jisha, and G. Assanto, Opt. Lett. **39**, 4317 (2014).
[20] J. Klaers, J. Schmitt, F. Vewinger, and M. Weitz, Nature **468**, 545 (2010).
[21] N. Ghofraniha, C. Conti, G. Ruocco, and S. Trillo, Phys. Rev. Lett. **99**, 043903 (2007).
[22] G. Assanto, T. Marchant, and N. F. Smyth, Phys. Rev. A **78**, 063808 (2008).
[23] S. Gentilini, F. Ghajeri, N. Ghofraniha, A. Di Falco, and C. Conti, Opt. Express **22**, 1667 (2014).
[24] G. Stegeman, G. Assanto, R. Zanoni, C. T. Seaton, E. Garmire, A. Maradudin, R. Reinisch, and G. Vitrant, Appl. Phys. Lett. **52**, 869 (1988).
[25] G. Vitrant, R. Reinisch, J. Paumier, G. Assanto, and G. Stegeman, Opt. Lett. **16**, 898 (1989).
[26] C. Conti, A. Fratalocchi, M. Peccianti, G. Ruocco, and S. Trillo, Phys. Rev. Lett. **102**, 083902 (2009).
[27] M. Leonetti, S. Karbasi, A. Mafi, and C. Conti, Phys. Rev. Lett. **112**, 193902 (2014).
[28] N. V. Tabiryan and B. Ya. Zeldovich, Mol. Cryst. Liq. Cryst. **62**, 237 (1980).
[29] M. Peccianti and G. Assanto, Phys. Rep. **516**, 147 (2012).
[30] F. W. Dabby and J. R. Whinnery, Appl. Phys. Lett. **13**, 284 (1968).
[31] F. Derrien, J. F. Henninot, M. Warenghem, and G. Abbate, J. Opt. A: Pure Appl. Opt. **2**, 332 (2000).
[32] J. E. Bjorkholm and A. A. Ashkin, Phys. Rev. Lett. **32**, 129 (1974).
[33] A. A. Zozulya and D. Z. Anderson, Phys. Rev. A **51**, 1520 (1995).
[34] E. A. Ultanir, G. Stegeman, C. H. Lange, and F. Lederer, Opt. Lett. **29**, 283 (2004).
[35] Y. Lamhot, A. Barak, O. Peleg, and M. Segev, Phys. Rev. Lett. **105**, 163906 (2010).
[36] A. Butsch, C. Conti, F. Biancalana, and P. S. J. Russell, Phys. Rev. Lett. **108**, 093903 (2012).

[37] W. Man, S. Fardad, Z. Zhang, J. Prakash, M. Lau, P. Zhang, M. Heinrich, D. N. Christodoulides, and Z. Chen, Phys. Rev. Lett. **111**, 218302 (2013).
[38] D. W. McLaughlin, D. J. Muraki, M. J. Shelley, and X. Wang, Physica D **88**, 55 (1995).
[39] A. Alberucci, A. Piccardi, M. Peccianti, M. Kaczmarek, and G. Assanto, Phys. Rev. A **82**, 023806 (2010).
[40] A. Alberucci and G. Assanto, Mol. Cryst. Liq. Cryst. **572**, 2 (2013).
[41] A. W. Snyder, S. J. Hewlett, and D. J. Mitchell, Phys. Rev. E **51**, 6297 (1995).
[42] M. Peccianti, A. Fratalocchi, and G. Assanto, Opt. Express **12**, 6524 (2004).
[43] I. Kaminer, C. Rotschild, O. Manela, and M. Segev, Opt. Lett. **32**, 3209 (2007).
[44] A. Piccardi, A. Alberucci, and G. Assanto, Phys. Rev. Lett. **104**, 213904 (2010).
[45] S. Ouyang and Q. Guo, Phys. Rev. A **76**, 053833 (2007).
[46] A. Alberucci and G. Assanto, J. Opt. Soc. Am. B **24**, 2314 (2007).
[47] Q. Guo, B. Luo, F. Yi, S. Chi, and Y. Xie, Phys. Rev. E **69**, 016602 (2004).
[48] J. J. Sakurai, *Modern Quantum Mechanics* (Addison-Wesley, Reading, MA, 1994).
[49] P. Aschiéri and V. Doya, J. Opt. Soc. Am. B **30**, 3161 (2013).
[50] M. Kwasny, A. Piccardi, A. Alberucci, M. Peccianti, M. Kaczmarek, M. A. Karpierz, and G. Assanto, Opt. Lett. **36**, 2566 (2011).
[51] Y. V. Izdebskaya, A. S. Desyatnikov, and Y. S. Kivshar, Phys. Rev. Lett. **111**, 123902 (2013).
[52] F. Maucher, E. Siminos, W. Krolikowski, and S. Skupin, New Journal of Physics **15**, 083055 (2013).
[53] P. B. Chappie, J. Staromlynska, and R. G. McDuff, J. Opt. Soc. Am. B **11**, 975 (1994).
[54] L. W. Casperson, A. Dittli, and T.-H. Her, Opt. Lett. **38**, 929 (2013).